Numerical simulation and optimization on opening angles of aerodynamic braking plates sets for a maglev train

Xiaofei Wang[1,2], Xiao Hu[2,3], Penghui Wang[2], Jun Zheng[2,3], Haitao Li[2,3], Zigang Deng[2,3*] and Weihua Zhang[2,3]

*Correspondence:
deng@swjtu.cn

[1] School of Mechanics and Aerospace Engineering, Southwest Jiaotong University, Chengdu 611756, China
[2] State Key Laboratory of Traction Power, Southwest Jiaotong University, Chengdu 610031, China
[3] Research Center for Super-High-Speed Evacuated Tube Maglev Transport, Southwest Jiaotong University, Chengdu 610031, China

Abstract

The aerodynamic braking has become an attractive option with the continuous improvement of train speeds. The study aims to obtain the optimal opening angles of multiple sets of braking plates for the maglev train. Therefore, a multi-objective optimization method is adopted to decrease the series interference effect between multiple sets of plates. And the computational fluid dynamics method, based on the 3-D, RANS method and SST k-ω turbulence model, is employed to get the initial and iterative data. Firstly, the aerodynamic drag and lift are analysed, as well as the pressure and velocity distribution of the flow field with the braking plates open at 75°. Then, the aerodynamic forces of each braking plate pre and post optimization are compared. Finally, the correlation between each set of braking plates and the optimized objective is analysed. It is found from the results that the aerodynamic drag and lift of the train have significant differences with or without multiple sets of braking plates. Additionally, the design variable corresponding to the number of iterations of 89 is taken as the relative optimal solution, and its opening angles of braking plates (B2-B5) are 87.41°, 87.85°, 87.41°, and 89.88°, respectively. The results are expected to provide a reference for the opening angles design scheme for the future engineering application of high-speed maglev train braking technology.

Keywords: Aerodynamic braking plates, Maglev train, Multi-objective optimization algorithm, Aerodynamic force

1 Introduction

There are a lot of braking issues that need to be solved with the rapid increase in operation speed of high-speed trains. Especially for maglev trains, conventional adhesive braking methods are restricted. Aerodynamic braking is a good technology to achieve non-adhesion braking by installing braking plates on top of the train, which has the advantages of environmental friendliness and high efficiency [1]. Meanwhile, it owns great performance because the aerodynamic braking force increases with the increase of operation speed. Therefore, it can be adopted as a supplement to braking methods such as adhesive braking and eddy current braking, especially for emergency braking under high-speed operation [2].

As for the research on the braking mechanism of aerodynamic braking, Japanese scholars are the leaders in this field and have carried out a lot of research based on wind tunnel experiments and real vehicle experiments [3, 4]. For example, taking a 500 km/h superconducting maglev train as the research object, the aerodynamic braking device was installed on the test vehicle MLU001 and several tests on the Yamanashi test line were subsequently carried out in 1988, as shown in Fig. 1. Extensive experimental data concerning on the aerodynamic braking characteristic was obtained in the test [5].

In recent years, scholars in China have begun researching aerodynamic braking technology for high-speed trains with numerical simulations, scaled models and full-scale experimental studies. Many literatures concentrated on the parameters of installation position and number, shape, different opening angles, braking plate height, axial and lateral spacing, and got the variation rule of braking force and proposed the corresponding design scheme [6–8]. Besides, some literatures studied the performance of aerodynamic braking under special circumstances, such as crosswind environment [9], bird impact [10] and aerodynamic noise [11]. Lots of research results demonstrated that aerodynamic braking was an effective and reliable emergency-braking technology in high-speed trains, and its implementation had also been achieved [12, 13].

In particular, the upstream braking plate will have an aerodynamic interference effect on the downstream braking plate when the train is equipped with multiple sets of braking plates [14]. Takami [15] combined the simulation and wind tunnel test and found that the drag of the braking plate was maximum at an opening angle of 75° to 85°, and there were a series of interference effects among the plates. Tian et al. [16] studied the braking force distribution of different numbers and positions of braking plates. It was found that the front plate would interfere with the braking force of the rear braking plates. Gao et al. [17] found that the maximum drag and comprehensive braking performance were best with the tablet shape and opening angle of 75°. Meanwhile, the interference effects of the height, axial spacing and lateral spacing of the front braking plate on the rear plates were studied. And they found that the aerodynamic interference effect is obvious when the axial distance between two rows of plates is less than 15 m. Niu et al. [18–21] studied and compared the interference effect of upstream aerodynamic braking on downstream aerodynamic braking with or without crosswind.

According to the existing research results, the interference effect can be decreased by adjusting the opening angles of braking plates. However, the current research about the opening angles of aerodynamic braking plates mainly focuses on optimizing the
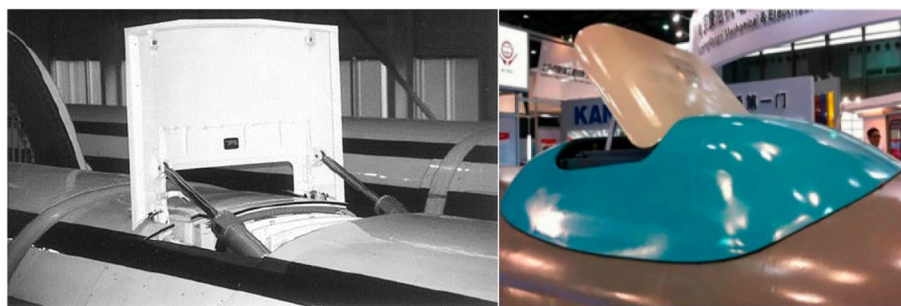

Fig. 1 Aerodynamic braking plates installed on the top of trains [5]

enumeration method for fewer conditions [15, 22]. Additionally, there is little research focused on the multiple optimizations of working conditions with lots of calculation data and research [23]. Therefore, a multi-objective optimization method is adopted to optimize the opening angles to decrease the series interference effect between multiple sets of aerodynamic braking plates. The maximum aerodynamic drag and minimum lift force are taken as the optimization objectives. At first, the computational fluid dynamics method is used to get the initial and iterative data, which has higher flexibility and meets the optimization requirements of this study. The results can offer a reference for the design scheme for the future engineering application of high-speed maglev train braking technology.

The remainder of this paper is organized as follows. Section 2 presents numerical simulations, including train models, computational domain, grid generation, grid independence analysis and verification. Section 3 presents the theory and progress of the multi-objective optimization method. In Section 4, the results and discussion, including force analysis, characteristics of the flow field and optimization calculation, are presented. Finally, some key conclusions are listed in Section 5.

2 Numerical simulation

2.1 Geometric models

As shown in Fig. 2, the train model used in numerical simulation is a full-size three-group high temperature superconductivity (HTS) maglev train composed of a head car, middle car, and tail car. To ensure the accuracy of numerical simulation, the simulation model retains the complex structure of the actual prototype as much as possible, including windshields and bogies. The overall length, width and streamline length of the train are about 61.36 m, 2.9 m and 12.98 m, respectively.
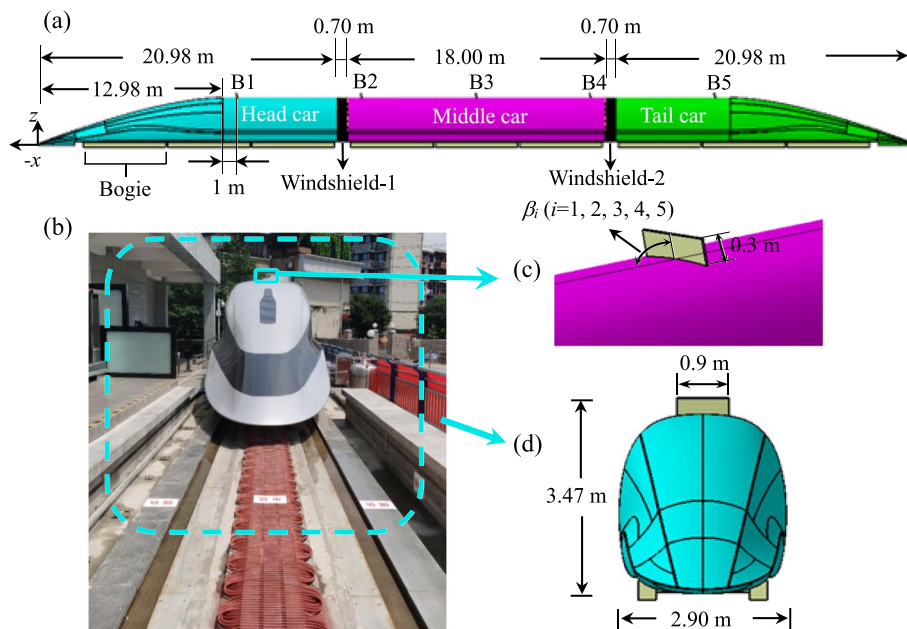

Fig. 2 The aerodynamic geometry model: (**a**) model of HTS maglev train; (**b**) vehicle prototype and test line; (**c**) parameters of the braking plate; (**d**) front view

The arrangement of braking plates is presented in Fig. 2(a). There are five rows of braking plates with the same size and configuration along the longitudinal centerline of the train, with a spacing of 8 m, which are installed on the top of the head, middle, and tail car. Besides, the rectangle braking plate is adopted and the dimensions are set to 0.9 m × 0.3 m × 0.03 m referring to the literature [24, 25]. For convenience, the five braking plates from head to tail are numbered B1 to B5 in sequence. The angle between the braking plate and the operation direction of the train is defined as opening angle β_i (i = 1, 2, 3, 4, 5). At the original state, the opening angle is set as 75° and the variation range is from 60° to 90°, according to the rules of optimal values of the single or multiple rows of braking plates referring to the literature [6, 15].

2.2 Computational domain

As shown in Fig. 3, the computational field of the train outflow field is established by referring to the related train aerodynamics literature [19]. The computational domain's length, height and width are 400 m, 40 m and 80 m, respectively. In addition, the inlet and outlet are designated as velocity-inlet and pressure-outlet, respectively. The surfaces of the train are defined as stationary no-slip walls. To simulate the ground effect efficiently, the ground surface is set as a slip wall and the slip velocity is equivalent reverse to the operation speed of the train. Then the top surface and both sides are set as symmetric planes.

To simulate the complex turbulent external flow field, the Reynolds-averaged Navier–Stokes equations (RANS) with the shear stress transport (SST) k-ω turbulence model was employed, and it is commonly used in this field of train aerodynamics [26, 27]. The SST k–ω model has a better prediction ability for low Reynolds number flows in the boundary layer and the complete turbulent flows outside the boundary layer. It is widely employed in the simulation of high-speed trains [28, 29]. A compressible flow solver is adopted since the velocity of the incoming flow is 600 km/h (Mach number 0.32). The convection and diffusion terms contained in the flow control equation are discretized by the second-order upwind and central difference schemes, respectively. To accelerate convergence, the semi-implicit method for pressure-linked equations consistent (SIMPLEC) is employed to process the pressure–velocity coupling.
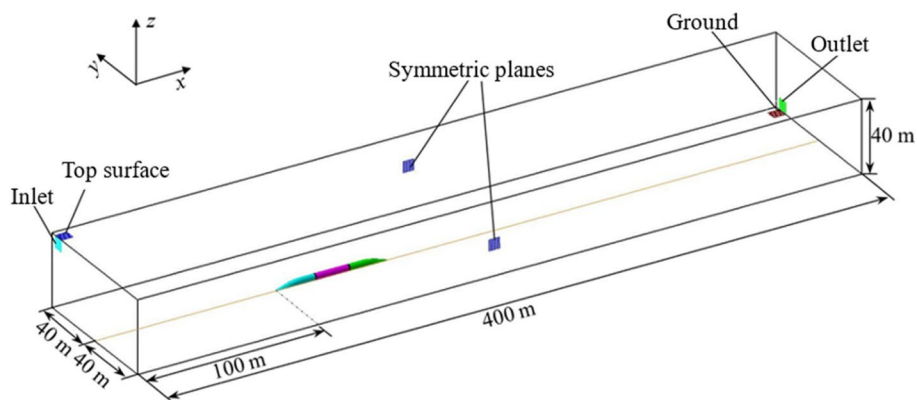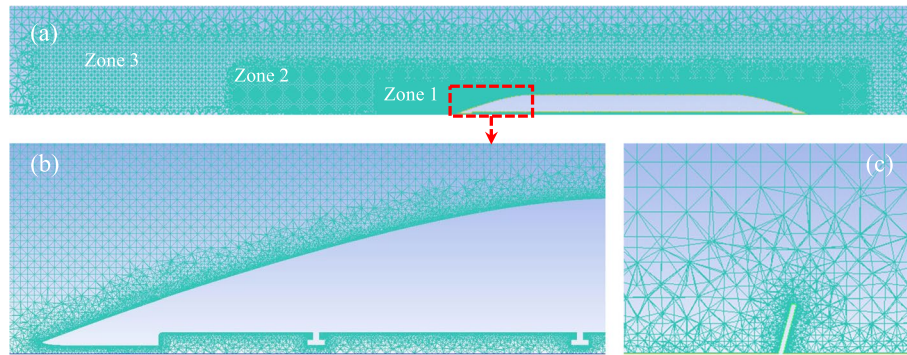

Fig. 3 Computational domain

Fig. 4 Configuration of medium computational mesh: (**a**) the mesh refinement zone; (**b**) the cross-section mesh around the streamline of the tail car; (**c**) the mesh around the braking plate

Table 1 The drag coefficient C_d of the maglev train under different mesh configurations

Items	Coarse	Medium	Fine
Number of meshes (million)	10.20	17.15	31.04
Drag coefficient C_d	0.2003	0.2025	0.2045
Relative error with fine mesh	1.958%	0.881%	—
Lift coefficient C_l	0.0624	0.0611	0.0581
Relative error with fine mesh	7.401%	5.164%	—

2.3 Grid generation

As shown in Fig. 4(a), the tetrahedral mesh provided by ICEM CFD is used to divide the computational domain. To capture the change of flow field structure near the train surface more accurately, the total thickness of the prism layer is set as 5.4 mm, the growth rate is 1.2 and the total layers is 8. Due to the complex flow structure around the train, especially in the braking plates and wake region, the multi-level refinement zone is utilized around the train referring to Muld [30] in Fig. 4. As shown in Table 1, three mesh configurations are used to obtain the appropriate mesh. The total number of corresponding meshes is 10.20 million, 17.15 million and 31.04 million, respectively. And the fine mesh contains 22 prism layers.

2.4 Mesh independence analysis

To select the appropriate mesh size, the aerodynamic drag coefficient and lift coefficient are compared with the difference between these three mesh configurations mentioned above. The drag coefficient (C_d) and lift coefficient (C_l) are defined as follows:

$$C_d = \frac{F_d}{0.5\rho A_F V^2}, \tag{1a}$$

$$C_l = \frac{F_l}{0.5\rho A_F V^2}. \tag{1b}$$

Where F_d and F_l are the aerodynamic drag and lift respectively; ρ is the air density, 1.225 kg/m^3 here; A_F is the maximum projected area of the maglev train, 7.81 m^2 here; and V is the operation speed, 600 km/h here.

It can be seen from Table 1 that there is little difference in the drag coefficient among these three mesh configurations. And the difference in lift coefficient between them is relatively large. But the relative error of middle mesh and fine mesh is within the reasonable range. Figure 5 shows the comparison of pressure on the top surface under different mesh configurations, and the trend of the pressure coefficient of Curve-1 of the three mesh configurations is consistent. However, the pressure of the coarse mesh is significantly different from that of the others around the tail car, while the pressure of the medium mesh and the fine mesh is consistent. Therefore, comprehensively considering the calculation accuracy and computing resources, the medium mesh size is adopted to carry out subsequent simulations in this study.

2.5 Algorithm validation

In the absence of direct experiment data, the indirect verification method of aerodynamic braking plates is employed to illustrate the reliability and accuracy of the numerical algorithm and results. Firstly, the numerical algorithm used in this study is consistent with other similar kinds of literature [31, 32], which could prove the reliability of this method in a sense. Secondly, an experiment similar to the plate sets adopted in this study was carried out by a wind tunnel in the Railway Technical Research Institute, which can be used for algorithm validation [15, 18]. As shown in Fig. 6, the dimensions of the computational domain and plates model used in the simulation are the same as the wind tunnel test models. The dimension of the test section of the wind tunnel is 3 m × 2.5 m, and the inflow velocity in the test is 111.1 m/s. The single plate's width, height and thickness are 0.5 m × 0.21 m × 0.003 m (angle 75°). The position of the plates is presented in Fig. 6(b). The three-component

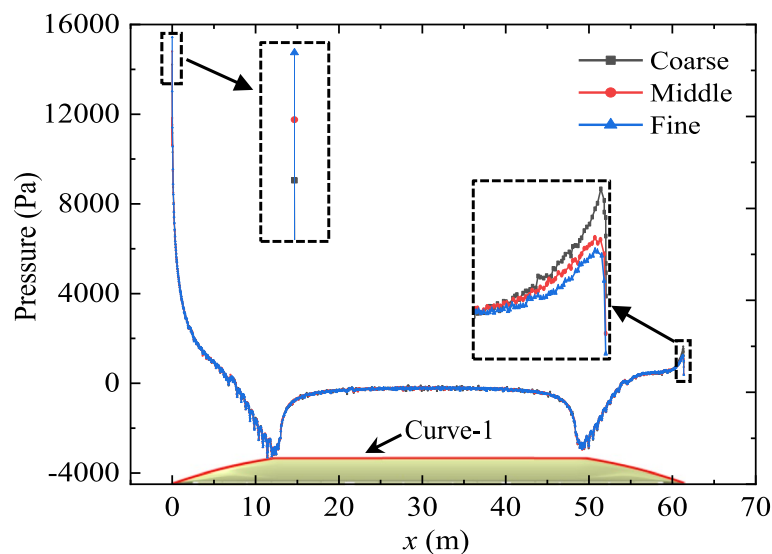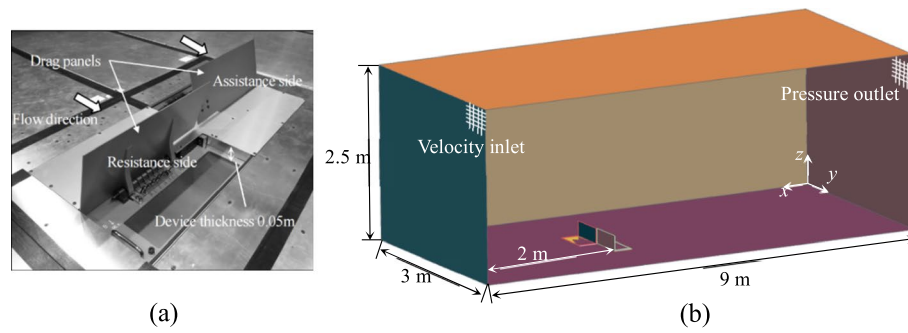**Fig. 5** Comparison of pressure under different mesh configurations

(a)   (b)

Fig. 6 Algorithm validation: (**a**) the test model and (**b**) the computational model [15]

Table 2 Comparison of aerodynamic drag of plates between wind tunnel test and numerical simulation

Items	Wind tunnel test [15]	Simulation	Error
Drag	1494 N	1578 N	5.62%

force sensors are used to measure the force of the plates mounted on the base. More detailed test parameters and settings can be found in the reference [15]. The grid generation in algorithm validation is the same as that in Section 2.3. The top, bottom, and two sides surfaces are defined as stationary walls. The front and back of the computational domain are designated as the velocity inlet and pressure outlet.

As shown in Table 2, the error of aerodynamic drag of the plates between the numerical simulation and the wind tunnel test is about 5%, which is within the permitted range of 10%. Therefore, it can be considered that the numerical method used in this study is reliable and the data is accurate.

3 Multi-objective optimization technique

3.1 Mathematical model

A standard multi-objective optimization problem usually contains two or more optimization objectives expressed by a mathematical expression as follows [33–35]:

$$
\begin{aligned}
&\min \ f_m(x), \ m = 1, 2, \cdots, M, \\
&\text{s.t. } x_k^L \le x_k \le x_k^U, \ k = 1, 2, \cdots, K,
\end{aligned}
\tag{2}
$$

where $f_m(x)$ represents the mth sub-objective function; M is the total number of sub-objective functions, 2 here; x_k is the kth design variable; x_k^L and x_k^U are the infimum and supremum values of the kth design variable, respectively; and K is the total number of design variables, 4 here. There is generally incompatibility among sub-objective functions, and it's almost impossible for multiple sub-objective functions to achieve the optimum at the same time. Therefore, it is necessary to coordinate the sub-objective functions of multi-objective optimization problems to achieve the relative optimum (Pareto optimal) [36]. As shown in Fig. 7, there are four definitions of Pareto concepts:
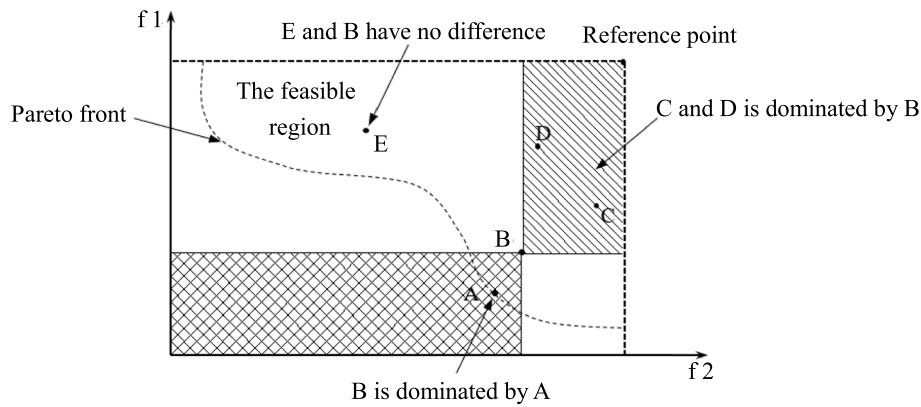
Fig. 7 The schematic diagram of concepts of Pareto dominance and Pareto front [37]

P1 (Pareto dominance): The x and x' are the feasible solutions that conform to the constraint condition of Eq. (2). And it is called as x dominates x' if $\forall i \in \{1, 2, \cdots, M\}, f_i(x) \le f_i(x')$ and $\exists j \in \{1, 2, \cdots, M\}, f_j(x) < f_j(x')$.

P2 (Pareto optimal): A feasible solution x is called to be Pareto optimal if it is not dominated by all other feasible solutions.

P3 (Pareto optimal solution set): The set of all Pareto optimal solutions in the design space.

P4 (Pareto front): The set of objective functions corresponding to the Pareto optimal solution set in the objective space.

So, the key to solving the multi-objective problem is to find the Pareto optimal solution. As one of the widely used non-normalized methods, the Second Generation of Non-Dominated Sorting Genetic Algorithm (NSGA-II) has the advantage of the elite retention strategy, based on a non-dominated sorting genetic algorithm (NSGA) to maintain the diversity of the population [37]. Due to the better convergence of the solution set and improved algorithm robustness and efficiency, the NSGA-II is employed to calculate the Pareto optimal solution of opening angles of multiple sets of braking plates.

3.2 Optimization progress

It is found that there is a series of interference effects between multiple sets of braking plates from the previous research. And the head car suffered the greatest drag at the angle of 75° of the braking plate in this study. Therefore, considering the inevitable aerodynamic interference of B1 and the limited computing resources, the opening angle of B1 is fixed to 75° and the opening angles of the other four sets of braking plates (B2-B5) are chosen to be optimized, and the adjustment value ranges from 60° to 90°. Meanwhile, the dimensionless intermediate variable b_i is defined as the design variable to facilitate the parameterization of the original design parameters as follows:

$$b_i = \frac{75(\beta_i - \beta_0)}{\beta_0}. \tag{3}$$

Where β_0 is the initial opening angle (75°) of the braking plate; β_i ($i = 2, 3, 4, 5$) is the opening angle of braking plates from B2 to B5; The value range of b_i is [-15, 15].

As in Fig. 8, the optimization process includes four steps. Step 1: Make the opening angles of braking plates automatically adjust by recording the macro file and parametric file in CATIA software and output new models. Step 2: Input the above output models and achieve meshing automatically by recording the macro file in ICEM CFD software and output mesh. Step 3: Input the above output mesh and start aerodynamic calculation automatically by recording the macro file in FLUENT software and output data. Step 4: In sequence, execute the progress of NSGA-II and judge if the result is the Pareto optimal solution by combing the input of corresponding optimization design variables, optimization objectives and scopes in ISIGHT software and output Pareto optimal solution or new command for CATIA to adjust opening angles of braking plates.

At the beginning of the optimization process, the train aerodynamic drag and lift are set as the optimization objectives. Besides, the opening angles of braking plates are set as the design variables with the NSGA-II method. Among them, the initial sampling number of the genetic algorithm population is 12, the number of evolutionary generations is 15, and a total of 180 aerodynamic calculations are performed.

4 Results and discussion

4.1 Aerodynamic force

Initially, Fig. 9 shows the comparison results of aerodynamic drag and lift with or without braking plates. It was found that the drag and lift forces of the train had significant differences with or without braking plates. The drag significantly increased by 55.84% and the lift force decreased by 22.72% with opening plates at 75°. Besides, the drag of the middle car had a maximum increase of 7765 N, and the tail car had a minimum increase of 1759 N. As for lift force, the negative lift force of the middle car changed to positive lift force by 5162 N distinctly. And the lift force of other parts was reduced obviously. Moreover, the reason why the aerodynamic drag increased was that the pressure
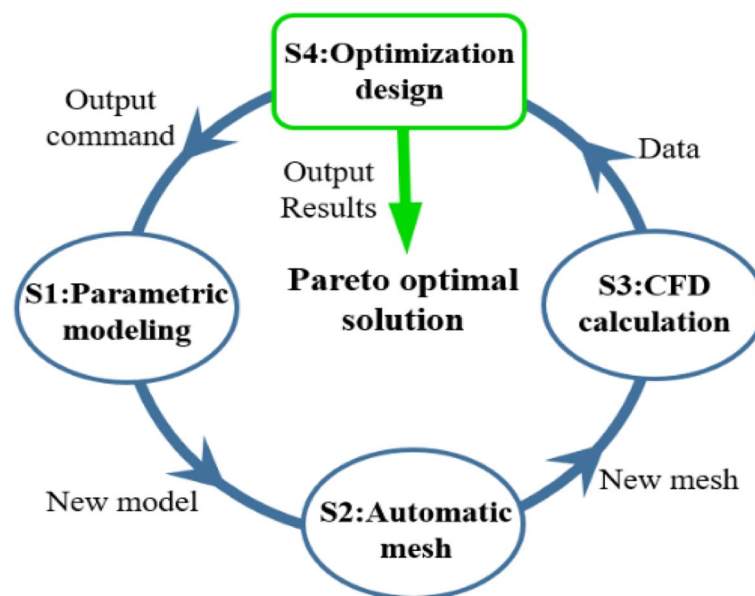

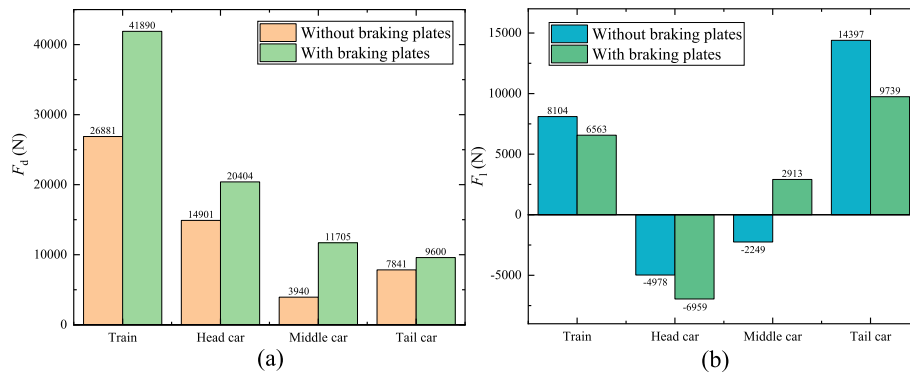**Fig. 8** The schematic diagram of the optimization process

Fig. 9 The comparison results of (**a**) aerodynamic drag and (**b**) lift with or without braking plates
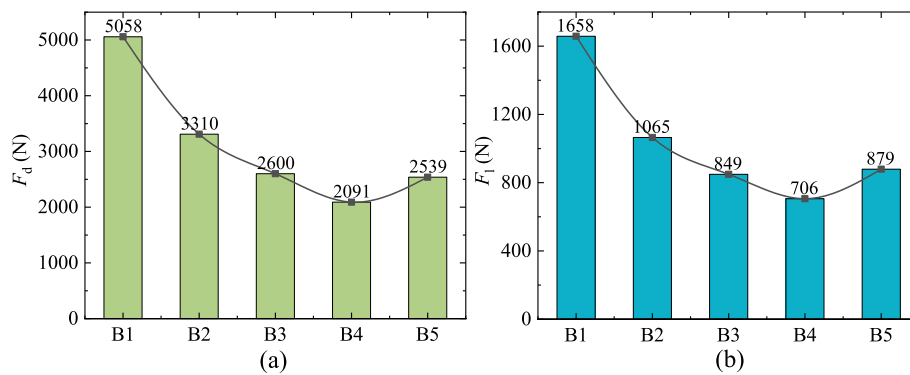

Fig. 10 The aerodynamic (**a**) drag and (**b**) lift of five groups of braking plates

difference increased due to the increasing windward area of the train with the opening braking plates. The same as the lift force, the top pressure increased, but the bottom pressure was not changed, and the aerodynamic lift decreased.

As shown in Fig. 10, the installation position of the braking plates has a great influence on the distribution of the flow field near the plates, and thus there are significant differences among the five groups of plates in aerodynamic drag and lift. It can be seen that the aerodynamic drag and lift of braking plates both decrease gradually from B1 to B4, and their decrease magnitude also decreases slightly. The aerodynamic force of B5 is slightly larger than that of B4. And the aerodynamic force of B1 located in the head car is the largest.

4.2 Structure of flow field

As shown in Fig. 11, the pressure distribution cloud diagram of the train and near braking plates was drawn to further analyze the change rules of aerodynamic force. As can be seen from it, a positive pressure area was formed on the windward of the first plate when the flowing air was blocked by the braking plate, and a negative pressure area was formed on the leeward. Thus, the pressure difference formed on the two sides of the braking plate was the main reason for the drag of braking plates. It can be also seen that the pressure difference between the windward and leeward of plate B1 had the largest value, and the airflow disturbance near the head car was also obvious, which made the
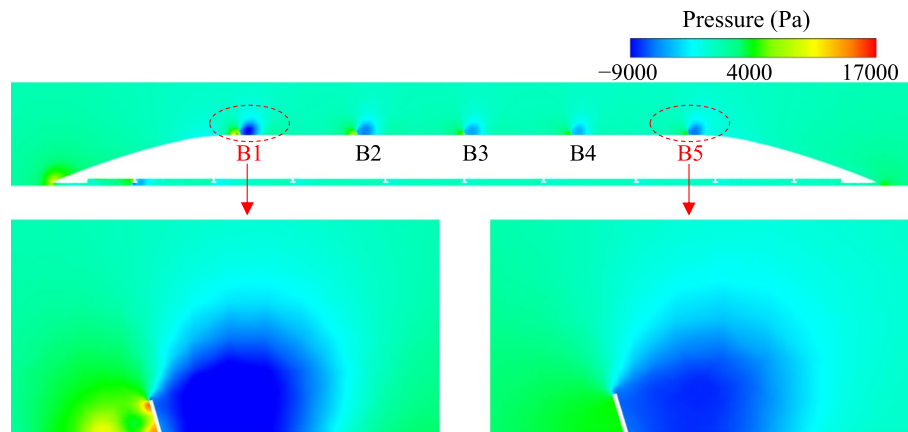
Fig. 11 The pressure distribution of maglev train and near braking plates
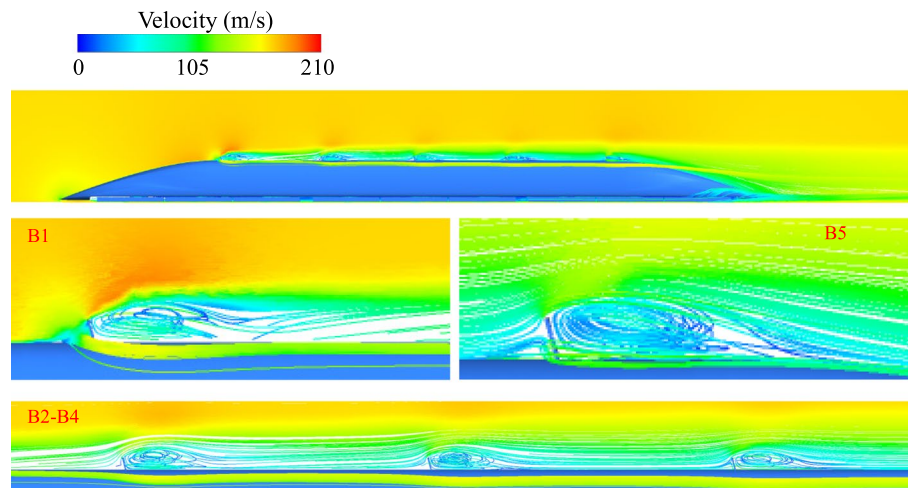

Fig. 12 The velocity distribution of longitudinal section of the train

aerodynamic drag of the head car change greatly. From B2 to B4, the four braking plates were not directly impacted by the head-on wind, and they were affected by the wake of the flow field of plate B1, so the pressure difference gradually decreased. At the same time, due to the large spacing between braking plate B5 and B4, the influence of the wake of the front flow field was reduced, so the pressure difference formed on the windward and leeward sides of B5 was relatively increased.

Figure 12 shows the velocity field distribution near the train and braking plates. The high-speed airflow in front of the head car was obstructed by the train nose and then separated, and part of it flowed along the head car streamline towards the tail car, and the other part swarmed into the bottom of the train. The top airflow obstructed by braking plates formed two vortexes and developed along two sides. In addition, while the airflow rises and accelerates above the braking plate, a separation flow formed downstream at the end of the braking plates, and then it will generate vortexes behind the plates and collapse, diffuse and subsequently reattach to the top surface. Therefore, the vortex generated by the front braking plate will influence the flow field at a long distance behind

the braking plate, resulting in a cascading interference effect between multiple sets of braking plates. As for B1, the energy of the top airflow decreased after being obstructed by the braking plate, and a low-speed flow field around the leeward side of B1 was generated. From braking plates B2 to B5, the airflow velocity around the rear plates decreased due to the rear plates being in the wake region of the front plates, and the intensity of the vortex generated also decreased.

Overall, opening the braking plates can not only increase the aerodynamic drag of the train but also reduce its lift force. The aerodynamic force of the braking plates is closely related to its location's pressure distribution and flow field structure. Thus, the braking effect of the downstream braking plate is weakened due to the influence of the flow field trails of the upstream plates on the downstream plate, while installing multiple braking plates on the train. Therefore, the opening angles of the braking plates can be reasonably adjusted to reduce the effect between multiple sets of plates and maximize the train's aerodynamic drag. Meanwhile, the lift force can adversely affect the stability of the levitation system of the maglev train, so, the aerodynamic lift of the maglev train needs to be limited.

4.3 Optimization solution

Figure 13 shows the historical curves of the changes of the design variables in the optimization process, where the red pentagram points represented the Pareto optimal solutions corresponding to the design variables obtained in the optimization process.
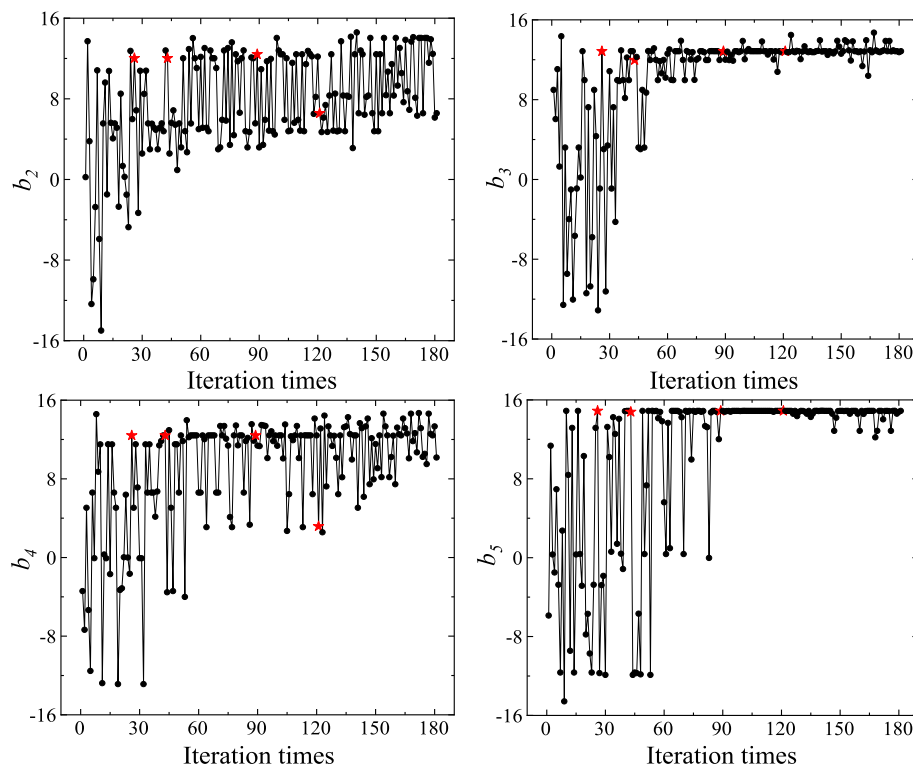

Fig. 13 The historical curves of the design variables in the optimization process

It can be seen that each optimized design variable tended to converge, and four sets of Pareto optimal solutions were obtained after the iterative calculation of the genetic algorithm, whose corresponding optimization objectives values are shown in Table 3.

Before optimization, the aerodynamic drag and lift of the train were 41.89 kN and 6.56 kN, respectively. It can be seen from Table 3 that the corresponding drag was the largest when the number of iterations was 89, which was about 2.22% higher than the drag at the initial angle. And the lift force decreased by about 17.02%. Moreover, the aerodynamic lift was the smallest when the number of iterations was 121, which was about 19.15% lower than the lift force at the initial angle, and the drag was increased by about 1.58%. Among the four sets of optimization results, there was little difference in the aerodynamic drag and lift between the number of iterations 89 and 121. For the adjustment of the braking plates opening angles, the primary target was to obtain the maximum aerodynamic drag and limit the lift force. Therefore, the design variables corresponding to the number of iterations of 89 were taken as the relative optimal solution, and its corresponding braking plates (B2-B5) opening angles are 87.41°, 87.85°, 87.41°, and 89.88°, respectively.

In the next part, the correlation between the design variables and the optimization objectives was obtained using Eq. (4), which was utilized to study the correlation between different braking plates and train aerodynamic force [38].

$$R = \frac{\sum\limits_{i=1}^{n}\left(X_i - \overline{X}\right)\left(Y_i - \overline{Y}\right)}{\sqrt{\sum\limits_{i=1}^{n}\left(X_i - \overline{X}\right)^2}\sqrt{\sum\limits_{i=1}^{n}\left(Y_i - \overline{Y}\right)^2}}. \tag{4}$$

Where $\overline{X}$ is the sample mean of X_i ($i = 1, ..., n$), and $\overline{Y}$ is the sample mean of Y_i ($i = 1, ..., n$).

From Fig. 14, the correlations of the design variables B2-B5 with the F_d are all positive. Among them, the strongest correlation is b_2, and the weakest is b_4, so the opening angle of plate B2 most influences the improvement of the train aerodynamic drag. It is seen that the correlations of B2-B5 with the F_l are all negative, where the strongest correlation is B4. And the weakest is B3. So, the reduction of train aerodynamic lift is most affected by the opening angle of plate B4. In addition, it is difficult to achieve the optimization objectives by changing a single design variable. Therefore, for the maglev train with multiple sets of braking plates, it is necessary to adjust the

Table 3 Design variables and corresponding optimization objectives values

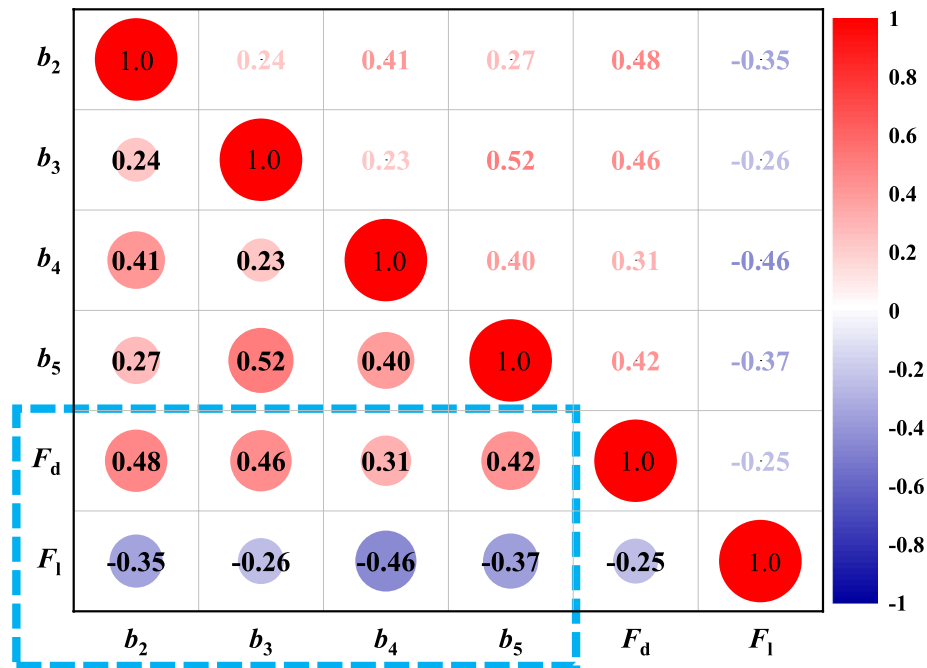| Iteration times	Design variables				Optimization objectives			
	b_2	b_3	b_4	b_5	F_d (kN)	Difference	F_l (kN)	Difference
0	0	0	0	0	41.89	0	6.56	0
26	12.02	12.85	12.41	14.88	42.68	+1.90%	6.14	-6.38%
43	12.02	11.97	12.41	14.78	42.42	+1.27%	5.72	-12.77%
89	12.41	12.85	12.41	14.88	42.82	+2.22%	5.44	-17.02%
121	6.57	12.85	3.17	14.88	42.55	+1.58%	5.31	-19.15%

Fig. 14 The correlation of design variables and optimization objectives
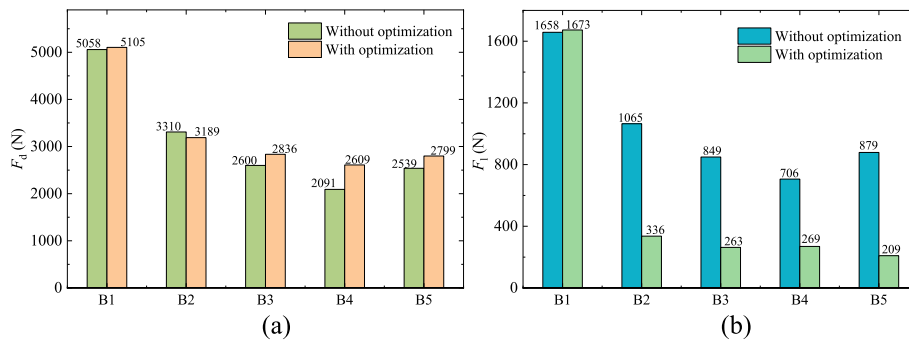

Fig. 15 The comparison of aerodynamic (**a**) drag and (**b**) lift force of braking plates pre and post optimization

opening angle of multiple sets of plates to achieve the braking effect of maximizing the aerodynamic drag and minimizing the aerodynamic lift for the maglev train.

Figure 15 showed the aerodynamic force comparison of braking plates pre and post optimization of opening angles. It is found that the aerodynamic drag and lift of B1 were still the maximum values compared with other plates and the overall trend of aerodynamic drag pre and post optimization kept consistent. As the pressure drag of B2 decreased, the aerodynamic drag decreased by about 121 N. And the pressure drags of B3, B4 and B5 increased, so the aerodynamic drag all increased. However, as shown in Fig. 15(b), the overall trend of aerodynamic lift with optimized opening angles was slightly different from that without optimization. Besides, the aerodynamic

lift of optimized plate B4 was larger than B3 and B5, proving that B4 had the greatest correlation to aerodynamic lift.

As shown in Fig. 16, the aerodynamic drag and lift forces of middle car and tail car have a significant improvement effect with optimization. Due to the lack of optimization of plate B1, the aerodynamic drag and lift forces of head car have no obvious improvement.

Figure 17 shows the pressure distribution of the braking plates pre and post optimization of opening angles. It is found that the optimized maximum and minimum pressure of plate B1 had a little difference with no optimization on account of the same opening angle, resulting in a slight change of pressure drag. In terms of plate B2, because the increased optimized maximum pressure of the windward was less than the absolute value of the decreased minimum pressure of the leeward, the pressure drag of B2 decreased. Additionally, for plate B3, the increased optimized maximum pressure of the windward was more than the absolute value of the decreased minimum pressure of the leeward, so the pressure drag of B3 increased. Similarly, the pressure drag for B4 and B5 increased.

5 Conclusions

To summarize, the optimal opening angles of multiple sets of aerodynamic braking plates for the maglev train were obtained by the multi-objective optimization method. There were some key results:

(1) The aerodynamic drag and lift of the train had significant differences with or without multiple sets of braking plates. Besides, the drag increased by 55.84% and the lift force decreased by 22.71% obviously with braking plates open at 75°.

(2) The top airflow obstructed by the braking plate created two vortexes and then developed along two sides. In addition, a separation flow formed downstream at the end of the plate and generated vortexes behind the plate. Therefore, the vortex generated by the front braking plates will influence the flow field at a long distance behind the plates, resulting in a cascading interference effect between multiple sets of braking plates. So the plate B1 has the best braking effect, and the braking force of B2 to B4 is reduced.

(3) The design variables corresponding to the number of iterations of 89 were taken as the relative optimal solution, and its corresponding braking plate (B2-B5) opening
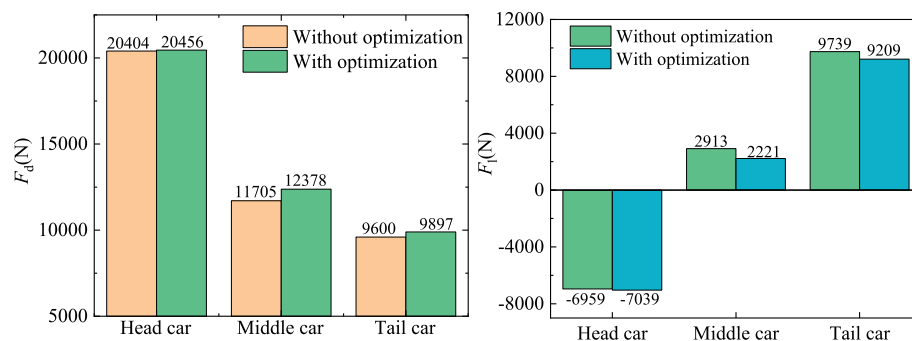

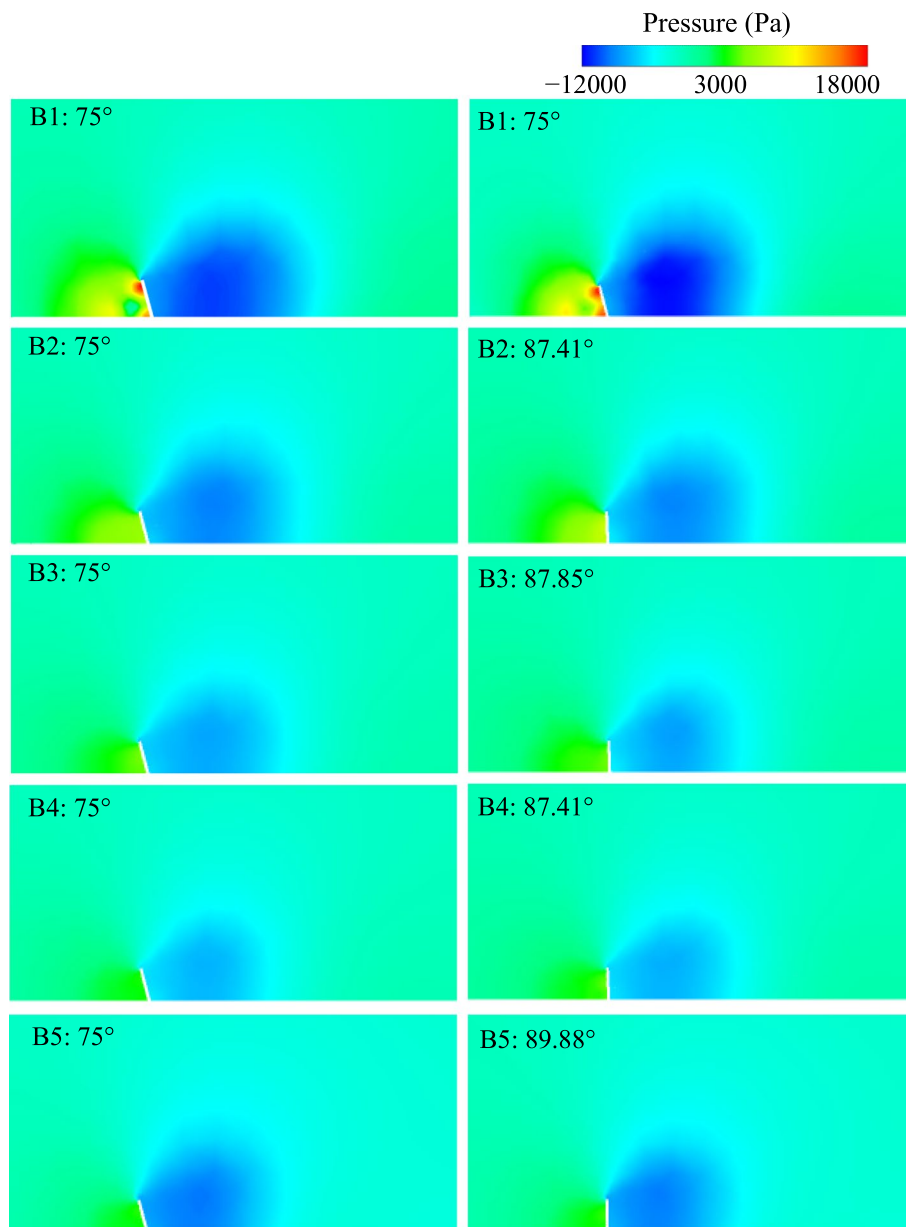**Fig. 16** The comparison results of aerodynamic (**a**) drag and (**b**) lift with or without braking plates

Fig. 17 The pressure distribution of braking plates pre and post optimization

angles were 87.41°, 87.85°, 87.41°, and 89.88°, respectively. The corresponding drag was about 2.22% higher than the initial angle, and the lift force decreased by about 17.02%. Moreover, the improvement of the train aerodynamic drag was most influenced by the braking plate B2, and the reduction of train aerodynamic lift was most affected by the braking plate B4.

In this study, only four groups of opening angles of braking plates (B2-B5) were optimized, primarily considering the limited computing resources. But real scenarios involved more complex parameters, like the installation position and number, shape, spacing distance, etc. This study only discussed the feasibility and applicability of the

multi-objective optimization method with CFD for the maglev train. Future studies should consider optimizing algorithms to reduce computational consumption to solve real engineering scenario problems. In conclusion, the results could be a reference for the opening angles design scheme for the future engineering application of high-speed maglev train braking technology.

Authors' contributions
XW was a major contributor in writing the manuscript and carried out the numerical simulation. XH directed the numerical simulation and put forward suggestions for the manuscript. PW and JZ processed the calculated data. HL drew some diagrams. ZD and WZ reviewed and revised the manuscript. All authors read and approved the final manuscript.

Availability of data and materials
The datasets used and/or analysed during the current study are available from the corresponding author on reasonable request.

Declarations

Competing interests
The authors declare no potential conflicts of interest with respect to the research, authorship, and/or publication of this article.

References

1. Baker CJ (2014) A review of train aerodynamics Part 1–Fundamentals. Aeronaut J 118(1201):201–228
2. Tian C, Weng JJ, Wu ML et al (2021) Review on test methods of aerodynamic brake for high-speed train. J Traffic Transp Eng 21(6):94–105
3. Shirakuni N, Endo Y, Takahashi K et al (2002) Overview of new vehicles for the Yamanashi Maglev Test Line. In: Proceedings of the 17th international conference on magnetically levitated systems and linear drives. Lausanne, http://maglev.ir/eng/documents/papers/conferences/maglev2002/topic5/IMT_CP_M2002_T5_S1_3.pdf
4. Takami H, Maekawa H (2017) Characteristics of a wind-actuated aerodynamic braking device for high-speed trains. J Phys Conf Ser 822:012061
5. Yoshimura M, Saito S, Hosaka S et al (2000) Characteristics of the aerodynamic brake of the vehicle on the Yamanashi Maglev Test Line. Q Rep RTRI 41(2):74–78
6. Gao LQ, Xi Y, Wang GH et al (2016) Opening angle rules of the aerodynamic brake panel. J Donghua Univ (English Edition) 33(1):20–24
7. Wu ML, Zhu YY, Tian C et al (2011) Influence of aerodynamic braking on the pressure wave of a crossing high-speed train. J Zhejiang Univ Sci A 12(12):979–984
8. Niu JQ, Wang YM, Wu D et al (2020) Comparison of different configurations of aerodynamic braking plate on the flow around a high-speed train. Eng Appl Comput Fluid Mech 14(1):655–668
9. Tian C, Wu ML, Zhu YY et al (2013) Running safety of high-speed train equipped with aerodynamic brake under cross wind. Adv Mat Res 614–615:348–354
10. Zuo JY, Zhu XY, Wu ML (2015) Numerical simulation of a bird impact on a composite aerodynamic brake wing of a high-speed train. Proc Inst Mech Eng F J Rail Rapid Transit 229(3):223–236
11. Wu P, Chen W, Shang WL et al (2012) Numerical simulation of aerodynamic noise based on the brake device of high speed trains. Chinese Q Mech 33(4):558–564
12. Puharic M, Linic S, Matic D et al (2011) Determination of braking force of aerodynamic brakes for high speed trains. Trans FAMENA 35(3):57–66
13. Puharic M, Matic D, Linic S et al (2014) Determination of braking force on the aerodynamic brake by numerical simulations. FME Trans 42(2):106–111
14. Zhang L, Li T, Zhang JY (2021) Effect of braking plates on the aerodynamic behaviors of a high-speed train subjected to crosswinds. Energies 14(2):401
15. Takami H (2013) Development of small-sized aerodynamic brake for high-speed railway. Trans Jpn Soc Mech Eng Ser B 79(803):1254–1263
16. Tian C, Wu ML, Fei WW et al (2011) Rule of aerodynamics braking force in longitudinal different position of high-speed train. J Tongji Univ Nat Sci 39(05):705–709

17. Gao LQ, Xi Y, Deng G et al (2015) Research on the aerodynamic interference effects of the brake panel. J Mach Des 32(9):19–24
18. Niu JQ, Wang YM, Liu F et al (2021) Numerical study on the effect of a downstream braking plate on the detailed flow field and unsteady aerodynamic characteristics of an upstream braking plate with or without a crosswind. Veh Syst Dyn 59(5):657–674
19. Niu JQ, Wang YM, Liu F et al (2020) Comparative study on the effect of aerodynamic braking plates mounted at the inter-carriage region of a high-speed train with pantograph and air-conditioning unit for enhanced braking. J Wind Eng Ind Aerodyn 206:104360
20. Niu JQ, Wang YM, Li R et al (2021) Comparison of aerodynamic characteristics of high-speed train for different configurations of aerodynamic braking plates installed in inter-car gap region. Flow Turbul Combust 106:139–161
21. Niu JQ, Wang YM, Chen ZW et al (2021) Numerical study on the effect of braking plates on flow structure and vehicle and enhanced braking of vehicles inside and outside tunnels. J Wind Eng Ind Aerodyn 214:104670
22. Bruce Ralphin Rose J, Vikraman M (2022) Enhancement of train braking efficiency by optimal flow control characteristics with aerodynamic braking system. Int J Interact Des Manuf 16(3):1273–1300
23. Lee M, Bhandari B (2018) The application of aerodynamic brake for high-speed trains. J Mech Sci Technol 32(12):5749–5754
24. Ghazanfari M, Tehrani PH (2014) Study on braking panels in high speed trains using CFD. Adv Railw Eng 2(2):93–105
25. Zuo JY, Wu ML, Tian C et al (2014) Aerodynamic braking device for high-speed trains: design, simulation and experiment. Proc Inst Mech Eng F J Rail Rapid Transit 228(3):260–270
26. Li T, Qin D, Zhang JY (2019) Effect of RANS turbulence model on aerodynamic behavior of trains in crosswind. Chinese J Mech Eng 32(1):85
27. Zhang J, Adamu A, Su XC et al (2022) Effect of simplifying bogie regions on aerodynamic performance of high-speed train. J Cent South Univ 29(5):1717–1734
28. Hu X, Deng ZG, Zhang WH (2021) Effect of cross passage on aerodynamic characteristics of super-high-speed evacuated tube transportation. J Wind Eng Ind Aerodyn 211:104562
29. Bao SJ, Hu X, Wang JK et al (2020) Numerical study on the influence of initial ambient temperature on the aerodynamic heating in the tube train system. Adv Aerodyn 2(1):28
30. Muld TW, Efraimsson G, Henningson DS (2012) Flow structures around a high-speed train extracted using proper orthogonal decomposition and dynamic mode decomposition. Comput Fluids 57:87–97
31. Morden JA, Hemida H, Baker CJ (2015) Comparison of RANS and detached eddy simulation results to wind-tunnel data for the surface pressures upon a class 43 high-speed train. J Fluids Eng 137(4):041108
32. Munoz-Paniagua J, García J, Lehugeur B (2017) Evaluation of RANS, SAS and IDDES models for the simulation of the flow around a high-speed train subjected to crosswind. J Wind Eng Ind Aerodyn 171:50–66
33. Zhang L, Zhang JY, Li T et al (2018) A multiobjective aerodynamic optimization design of a high-speed train head under crosswinds. Proc Inst Mech Eng F J Rail Rapid Transit 232(3):895–912
34. Deb K (1999) Multi-objective genetic algorithms: problem difficulties and construction of test problems. Evol Comput 7(3):205–230
35. Aguilar Madeira JF, Rodrigues H, Pina H (2005) Multi-objective optimization of structures topology by genetic algorithms. Adv Eng Softw 36(1):21–28
36. Burke EK, Kendall G (2014) Search methodologies: introductory tutorials in optimization and decision support techniques. 2nd Ed. Springer: New York. https://link.springer.com/book/10.1007/0-387-28356-0
37. Deb K, Pratap A, Agarwal S et al (2002) A fast and elitist multiobjective genetic algorithm: NSGA-II. IEEE Trans Evol Comput 6(2):182–197
38. Schober P, Boer C, Schwarte LA (2018) Correlation coefficients: appropriate use and interpretation. Anesth Analg 126(5):1763–1768

Publisher's Note

Springer Nature remains neutral with regard to jurisdictional claims in published maps and institutional affiliations.